卒業論文

Finite Element Analysis of out plane buckling phenomenon exhibited by semiconductor nanoscale structures

半導体の微細素子構造の面外座屈に関する有限要素法解析

p. 1~p. 55 完

平成 25 年 2 月 1 日提出

指導教員　泉　聡志　准教授

110203　シー　ロンチュン

Contents

Chapter 1. Introduction 5

1.1 Background and Motivation 5

1.1.1 Introduction 5

1.1.2 Semiconductor structure and fabrication process 5

1.1.3 Trends and emerging problems in semiconductor industry 8

1.1.4 Background research 11

1.2 Objectives and outline of research 13

Chapter 2. 1 Layer Thin Plate Model 14

2.1 Introduction 14

2.2 Föppl von Kármán Equations for thin elastic plates 14

2.3 Finite element analysis of 1 Layer Model 20

2.3.1 Description of model schematics 20

2.3.2 Assessment of the length for models 24

2.3.3 Comparison of simulation results with theoretical values at various width to height ratios 25

Chapter 3. The 2 Layer Thin Plate Model 27

3.1 Introduction 27

3.2 Finite Element Analysis of 2 Layer Model 28

3.2.1 Description of model schematics 28

3.2.2 Inconsistency of initial FEM results with experimental results 30

3.2.3 Discussion of areas of interest and governing factors 33

3.3 Factors affecting λ and $\sigma_{critical}$ 35

3.3.1 Relationship of λ and $\sigma_{critical}$ with respect to h 35

3.3.2 Relationship of λ and $\sigma_{critical}$ with respect to l 36

3.3.3 Relationship of λ and $\sigma_{critical}$ with respect to l_m/l 38

Chapter 4. Comparison of experimental and FEM results 39

4.1 Introduction 39

4 . 2 Finding the values $l_{critical}$ 40

4 . 2 . 1 Relationship between λ/l and l_m/l 40

4 . 2 . 2 Calculating $l_{critical}$ from λ and l_m relationships 42

4 . 2 . 3 Discussion of results for $l_{critical}$ obtained from l (l_m, λ) 43

4 . 2 . 4 Calculating $l_{critical}$ from $\sigma_{critical}$ and l_m 45

4 . 2 . 5 Discussion of results of obtained from σ (l_m, h, l) 46

Chapter 5. Conclusion 49

5 . 1 Summary of results 49

5 . 2 Suggestions for future research 51

References 52

Acknowledgements 53

List of Figures

Fig. 1-1 Semiconductor fabrication process [1]. 7
Fig. 1-2 Graph showing Moore's law: doubling of transistors as process nodes scale down [2].. 8
Fig. 1-3 Half pitch of a memory chip [3]. 9
Fig. 1-4 Periodic wave like buckling patterns in line and space structure of semiconductors [5]. 10
Fig. 1-5 Strip geometry of swelling gel, T.Mora [6]. 11
Fig. 1-6 Experimental Data scatter plot against theoretical data [6]. 12
Fig. 2-1 Deformation in thin plates. 14
Fig. 2-2 Stability Diagram at Poisson's ratio =0.5, T.Mora [7]. 19
Fig. 2-3 Full 1 layer thin plate model. 21
Fig. 2-4 Up close of one end of 1 layer model. 21
Fig. 2-5 Single element depicting intrinsic stress applies via inistate command. .. 21
Fig. 2-6 First buckling mode of 1 layer model at $h/l = 0.1$. 23
Fig. 2-7 Top view of buckled 1 layer model. 23
Fig. 2-8 Graph of $\sigma_{critical}$ and λ upon varying L/l. 24
Fig. 2-9 Graph of difference between FEM and theoretical values of $\sigma_{critical}$ and λ at varying h/l. 25
Fig. 3-1 Full 2 layer thin plate model. 28
Fig. 3-2 Up close of one end of 2 layer model. 29
Fig. 3-3 Material Properties of 2 layer Model in experiments. 30
Fig. 3-4 Change in variables during semiconductor etching process. 33
Fig. 3-5 Graph of λ and $\sigma_{critical}$ upon varying h. 35
Fig. 3-6 Graph of λ and $\sigma_{critical}$ upon varying l. 36
Fig. 3-7 Graph of λ and $\sigma_{critical}$ upon varying l_m/l. 38
Fig. 4-1 Figure showing the etching process at which when $l_{critical}$ occurs............. 39
Fig. 4-2 Graph of relationship between λ/l and l_m/l at various h/l. 40
Fig. 4-3 Graph of relationship between λ/l and l_m/l for experimental and Ansys (FEM) results. 41
Fig. 4-4 Graph of average λ/l against l_m/l with error bars. 42
Fig. 4-5 3D surface graph of $\sigma_{critical}$, l_m/l and h/l. 45
Fig. 4-6 Change in h according to etching depth l. 48

List of tables

Table 2-1 Finite Element Analysis Conditions. 22

Table 3-1 FEM analysis conditions. 29

Table 3-2 Comparison of experimental results and simulation results. 31

Table 3-3 h/l and l_m/l of experimental results. 34

Table 4-1 Predicted values of $l_{critical}$ and the corresponding $\sigma_{critical}$. 43

Table 4-2 Predicted values of $l_{critical}$ and the corresponding $\lambda_{critical}$. 46

Chapter 1. Introduction

1.1 Background and Motivation

1.1.1 Introduction

The importance of semiconductors in human lives is more often than not left unappreciated. Semiconductor enables our computers, smart phones, medical systems and many other electronic devices that are necessary in our lives. As people will continue to demand higher standards of living along with the improvement of technology, semiconductors will continue to play an important role in the future.

Semiconductors are materials that have an immediate electrical conductivity between conductors and insulators. Semiconductors integrated circuits are the basic foundation of the electronics industry due to their ability to change their electrical conductivity upon varying conditions. Today, silicon is the dominant semiconductor material used in integrated circuits due to their wide bandwidth, low cost and ability to be oxidized readily to form high quality silicon dioxide insulator.

1.1.2 Semiconductor structure and fabrication process

IC fabrication technology is a planar process that takes place over the whole plane of a silicon wafer. Fig 1-1 below shows the major steps of semiconductor fabrication.

The various steps are as follows:

a) A bare n-type silicon substrate.

b) The conducting layer is either deposited by chemical vapor deposition or the silicon substrate could be oxidized to form silicon dioxide. In Fig 1-1, the latter is shown. In most instances, an additional layer of thin film may be deposited above the silicon dioxide/conducting layer. This is especially true for memory chips such as NAND and DRAM.

   The next 3 steps from c) to e) are known as photolithography. Photolithography is a patterning process used to define the geometry of the semiconductor.

c) Ultraviolet light sensitive photo resist is applied to the silicon dioxide layer.

d) The wafer is exposed to UV light through a pattern mask.

e) The photo resist on exposed areas are washed away and while those under opaque areas remain.

f) The silicon dioxide layers without photo resist are then etched away by gaseous chemicals.

g) The remaining photo resist is then washed away. The structure seen in here is known as the line and space pattern.

h) Finally, the junctions are formed by implanting ions and contact points are formed by coating the layers with a layer of metal film.

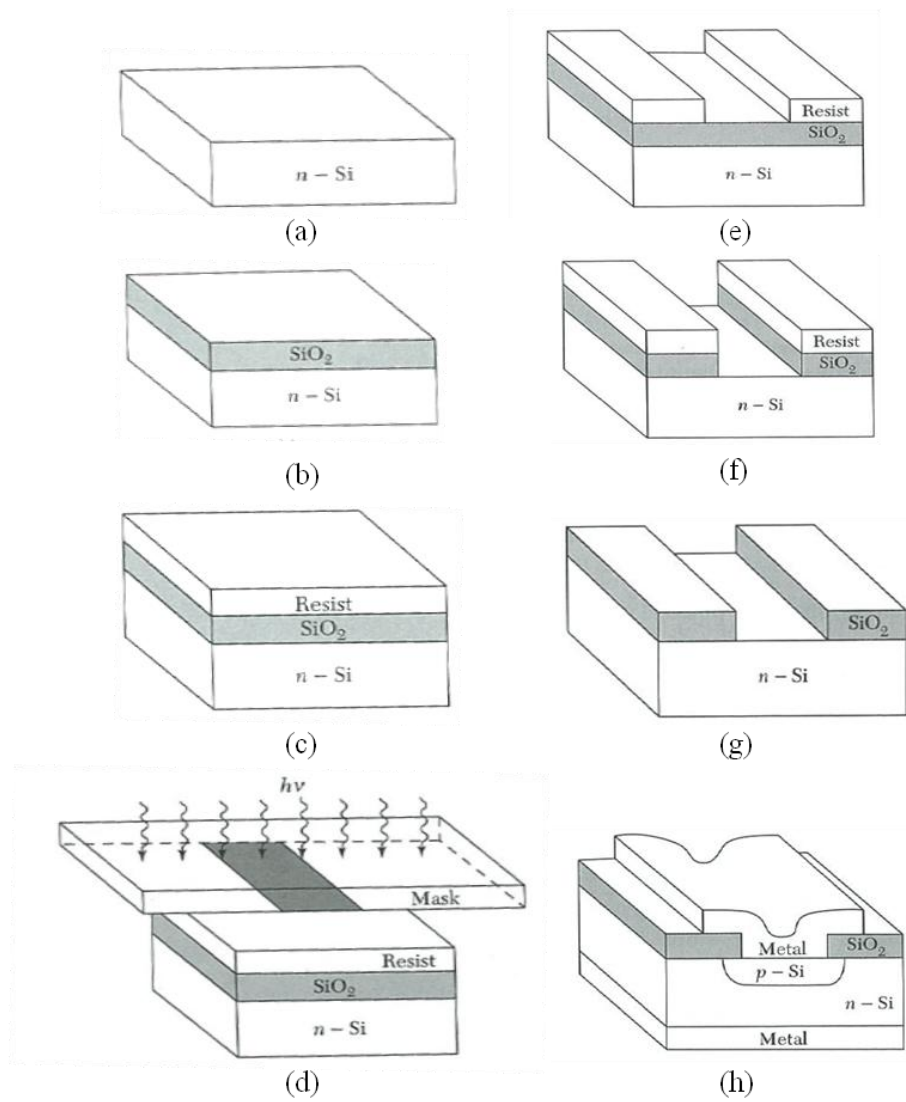

Fig. 1-1 Semiconductor fabrication process [1].

1.1.3 Trends and emerging problems in semiconductor industry

The roadmap of the semiconductor and electronics industry is mapped out by Moore's law, a prediction that the number of transistors on a silicon wafer will double with every production cycle (18 months – 24 months) [2]. Fig. 1-2 shows a graph of number of transistors on a silicon wafer against the years and nodes. This increase in number of transistors is a result of decreasing element size, also known process nodes. The actual definition of process nodes tend to vary with semiconductor companies and countries but is most commonly defined as the half pitch of a semiconductor, the distance across half the element and half the channel. Fig. 1-3 below shows the definition of a half pitch.

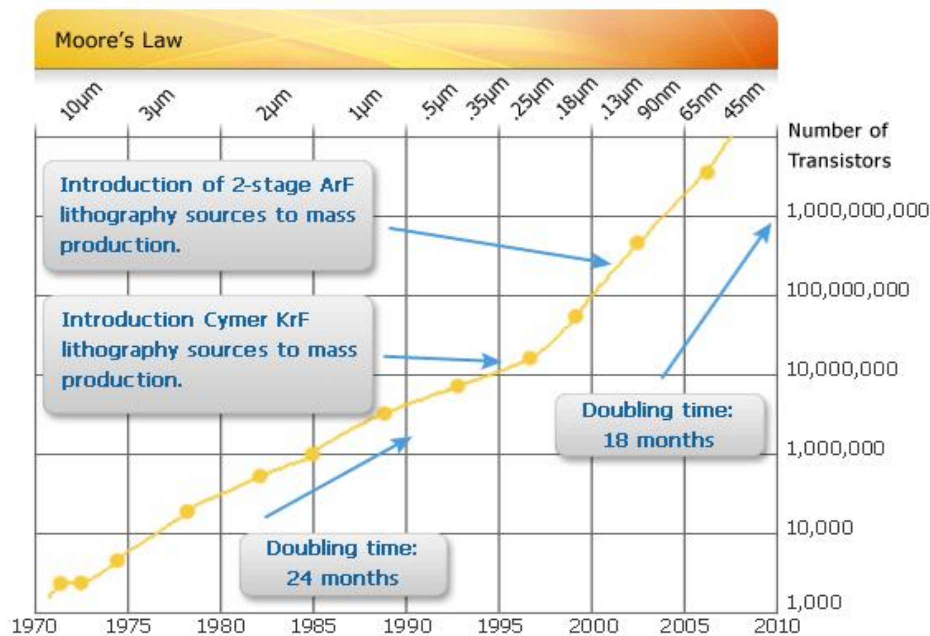

Fig. 1-2 Graph showing Moore's law: doubling of transistors as process nodes scale down [2].

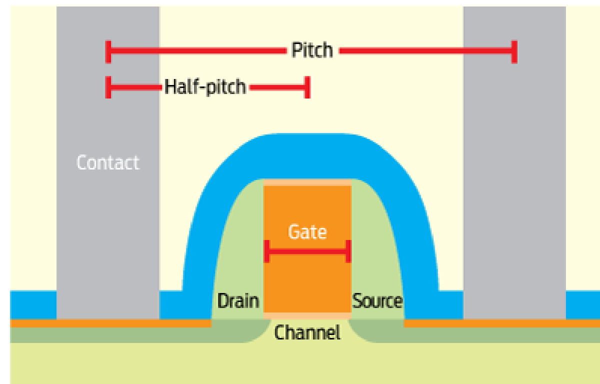

Fig. 1-3 Half pitch of a memory chip [3].

Smaller process nodes enable electronic devices to have higher processing power, lower power consumption, lower production costs and smaller form factor. This has led to the evolution of mobile devices such as smart phones, tablet computers and gaming devices. As the half pitch decreases, the width of the semiconductor element also decreases, but the height of the element does not decrease proportionally. The height has not changed much despite decreasing process nodes as there needs to be a certain height to ensure sufficient resistance between the channels and contact points. As a result, the ratio of width to height of the elements decreases along with process nodes.

The decreasing width to height ratio has led to lower mechanical strength in the semiconductor elements and signs of mechanical deformation (buckling) during the etching process (Fig. 1-1(f)) has been observed in recent years. The driving force for this deformation is the residual stress formed during the deposition phase (Fig. 1-1(b)). Residual stress can be divided into two types, thermal stress and intrinsic stress. Deposition usually occurs at a high temperature, and

upon cooling, the difference in the thermal expansion rates between the substrate and the deposited material causes thermal stress. On the other hand, intrinsic stress is a form of residual stress which arises during deposition processes and is already present at deposition temperature. There are various mechanisms for the formation of intrinsic stress such as vacancy annihilation, grain growth phase transition and difference in lattice spacing's of the substrate and deposited layer [4].

As a result of the stress and lowered mechanical strength, periodic waves are formed in the line and space structures as shown in Fig. 1-4, instead of the straight line and space structures seen in Fig. 1-1(g). This periodic shape causes the neighboring elements to touch, creating short circuits within the chip, undermining its quality.

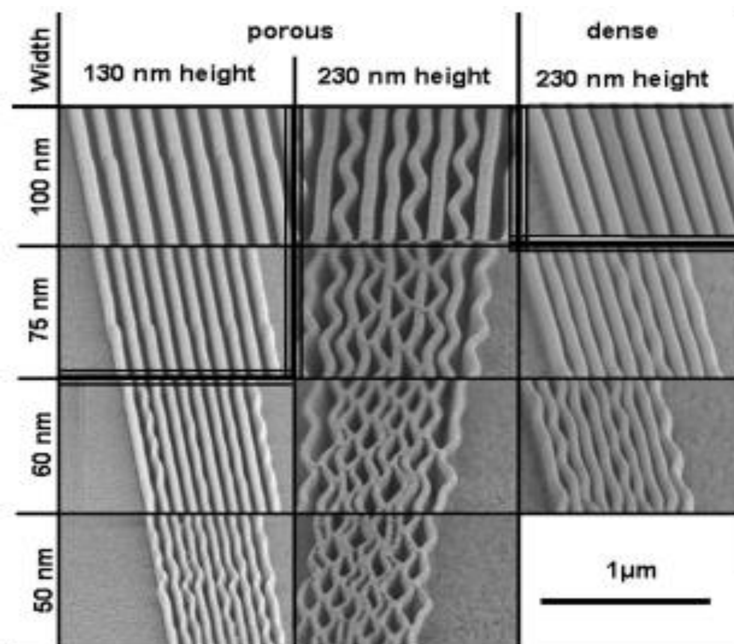

Fig. 1-4 Periodic wave like buckling patterns in line and space structure of semiconductors [5].

1.1.4 Background research

Prior research on 1 layer thin plate buckling has been conducted on swelling gels with different properties and their wavelengths, λ have been studied [6]. The experiment conducted involved a strip of soft gel being attached to a strip of stiff gel and immersed into water as shown in Fig. 1-5. Due to the different elastic and swelling properties, stress is generated as the soft swelling gel absorbs water, causing it to bend out of plane (z-direction), forming periodic wave like patterns.

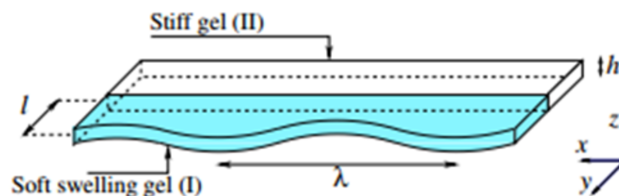

Fig. 1-5 Strip geometry of swelling gel, T.Mora [6].

The experimental results obtained were consistent with the theoretical results above a critical length and were able to predict the wavelengths to a consistent degree above height to width ratios of 3 to 4 as shown in Fig. 1-6.

However, the research was focused on the predicting λ for 1 layer models, and did not delve further into the prediction of the stress in the plate at which buckling occurs or for multilayer models.

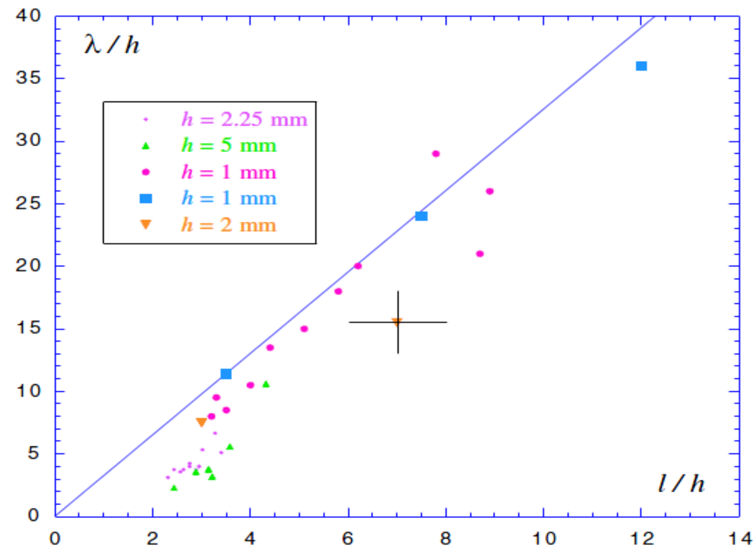

Fig. 1-6 Experimental Data scatter plot against theoretical data [6].

Research has also been done in attempting predict the buckling coefficient of multilayer models at varying element heights [5]. However, the research did not touch upon the relationship the buckling coefficient have with the mask height and width. The research also did not delve further into studying the wavelength and amplitude of the buckled structure.

In conclusion, the previous research has not made clear the characteristics of the buckling phenomenon, and the factors governing the buckling wavelength and stress.

1 . 2 Objectives and outline of research

In aim of improving the framework for the design of semiconductor nanoscale structures to prevent buckling phenomenon, the objective of this research is to make clear the characteristics of the buckling mechanism in 2 layer thin plates and the factors affecting the buckling wavelength and stress. This shall be achieved through the use of Finite Element Method (FEM) analysis to simulate the buckling phenomenon.

The following researches are proposed in order to achieve the main objective.

1) Based on a thin plate theory, create an accurate finite element model.

   Prior to studying 2 layer thin plate models that can simulate the buckling phenomenon in semiconductors, it is important to confirm the correct boundary and force conditions to be used. Given the availability of theoretical equations for the 1 layer model, these equations are used to validate a 1 layer model.

2) Simulate the buckling phenomenon in 2 layer models and study the relationships between the various structural parameters, wavelength and stress at which buckling occurs.

   FEM analysis of the 2 layer model will be conducted and relationship equations shall be drawn from the results. Comparison with the experimental data would give us an insight on the accuracy of these equations and the shortcomings of FEM analysis.

Chapter 2. 1 Layer Thin Plate Model

2.1 Introduction

Semiconductors have small width to height ratios and can be considered as thin flat plates. This chapter aims to explore the theory of the buckling phenomenon of 1 layer thin plates and compare them with FEM simulation results.

Chapter 2.2 will explain the theoretical equations behind thin plate deformation and Chapter 2.3 will highlight the simulation results from FEM analysis and compare them with the theoretical equation.

2.2 Föppl von Kármán Equations for thin elastic plates

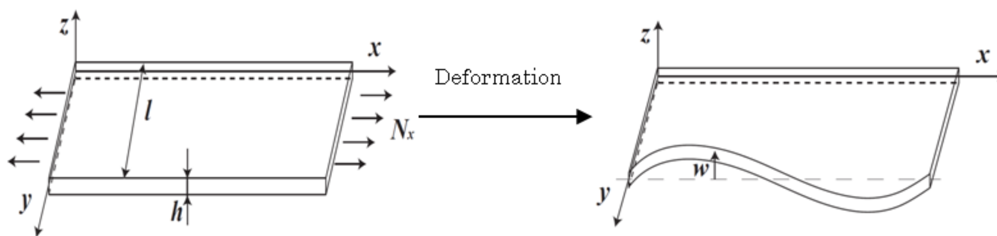

Fig. 2-1 Deformation in thin plates.

l: height of plate; h: width of plate; N_x: external force; w: out plane displacement

Upon external force N_x or internal stress σ, out plane displacement occurs in thin plates as shown in Fig. 2-1. This out plane deflection is governed by a set of nonlinear partial differential equations known as the Föppl von Kármán equations [7]. These equations are derived from the

force, moments and stress equations in an elastic plate with residual strains.

The following 2 assumptions are necessary for this equation: 1) the height of the model, l must be significantly greater than its width, h (i.e. the width to height ratio, h/l must be significantly small); 2) the out plane displacement, w must be sufficiently small.

The Föppl von Kármán equations are as follows [7]:

$$D\Delta^2 w - h\frac{\partial}{\partial x_\beta}\left(\sigma_{\alpha\beta}\frac{\partial w}{\partial x_\alpha}\right) = 0 \tag{2.1}$$

$$\mathrm{D} = \frac{Eh^3}{12(1-v^2)}$$

$$\frac{\partial \sigma_{\alpha\beta}}{\partial x_\beta} = 0 \tag{2.2}$$

where $w(x,y)$ is the out plane displacement; h is the width of the plate in the y-direction; $\sigma_{\alpha\beta}$ is the in plane stress tensor; E is the Young's modulus of the material; v is the Poisson's ratio of the material. D is a function of the Young's modulus and the Poisson's ratio and is known as the bending stiffness.

Expanding Eq. (2.1), we get Eq. (2.3)

$$\mathrm{D}\Delta^2 w - h\left\{\left(\frac{\partial \sigma_{xx}}{\partial x}\frac{\partial w}{\partial x} + \sigma_{xx}\frac{\partial^2 w}{\partial x^2}\right) + \left(\frac{\partial \sigma_{xy}}{\partial y}\frac{\partial w}{\partial x} + \sigma_{xy}\frac{\partial^2 w}{\partial xy}\right) + \left(\frac{\partial \sigma_{yx}}{\partial x}\frac{\partial w}{\partial y} + \sigma_{yx}\frac{\partial^2 w}{\partial xy}\right) + \left(\frac{\partial \sigma_{yy}}{\partial y}\frac{\partial w}{\partial y} + \sigma_{yy}\frac{\partial^2 w}{\partial y^2}\right)\right\} = 0$$

$$\mathrm{D}\Delta^2 w - h\left\{\frac{\partial w}{\partial x}\left(\frac{\partial \sigma_{xx}}{\partial x} + \frac{\partial \sigma_{xy}}{\partial y}\right) + \frac{\partial w}{\partial y}\left(\frac{\partial \sigma_{yx}}{\partial x} + \frac{\partial \sigma_{yy}}{\partial y}\right) + \sigma_{xx}\frac{\partial^2 w}{\partial x^2} + \sigma_{xy}\frac{\partial^2 w}{\partial xy} + \sigma_{yy}\frac{\partial^2 w}{\partial y^2}\right\} = 0 \tag{2.3}$$

Similarly, Eq. (2.2) can be expanded to give the following 2 equations,

$$\frac{\partial \sigma_{xx}}{\partial x} + \frac{\partial \sigma_{xy}}{\partial y} = 0 \tag{2.4}$$

$$\frac{\partial \sigma_{yx}}{\partial x} + \frac{\partial \sigma_{yx}}{\partial y} = 0 \tag{2.5}$$

Substitute Eqs. (2.4) and (2.5) into Eq. (2.3),

$$\mathrm{D}\Delta^2 w - h\left(\sigma_{xx}\frac{\partial^2 w}{\partial x^2} + \sigma_{xy}\frac{\partial^2 w}{\partial xy} + \sigma_{yy}\frac{\partial^2 w}{\partial y^2}\right) = 0 \tag{2.6}$$

As we only consider the stress to work in the *x*-direction, σ_{xy} and σ_{yy} is assumed to be zero.

We arrive at Eq. (2.7)

$$\mathrm{D}\Delta^2 w - h\sigma_{xx}\frac{\partial^2 w}{\partial x^2} = 0 \tag{2.7}$$

Next, the following substitutions are carried out to make the physical quantities dimensionless.

$$X = \frac{x}{l}, Y = \frac{y}{l} \text{ where } l \text{ is the unit length}$$

$$P = \frac{-\sigma_{xx} h l^2}{D} = \frac{-\sigma_{xx} E}{12(1-v^2)}\left(\frac{h}{l}\right)^2 \tag{2.8}$$

$$\text{where } \frac{D}{hl^2} \text{ is the unit stress}$$

$$\Delta^2 w - P\frac{\partial^2 w}{\partial x^2} = 0\,, P = \frac{12(1-v^2)l^2}{h^2} \tag{2.9}$$

P is the compressive non-dimensional stress applied uniformly along the *x*-direction within the plate and is proportional to the squared of the width to height ratio as seen in Eq. (2.8).

Next, we assume that the out plane displacement is governed by a sinusoidal function with wave number *q*. Where *q* is the non-dimensional wave number of the plate and is inversely proportional to the height of the plate.

$$w(X,Y) = \xi(Y)\cos qX \tag{2.10}$$

where $q = \frac{2\pi}{l}\lambda$

Substituting Eq. (2.10) into Eq. (2.9), we get Eq. (2.11)

$$\xi^{(4)} - 2q^2\xi^{(2)} + (q^4 - Pq^2)\xi = 0 \tag{2.11}$$

Eq. (2.11) is a fourth order linear differential equation and has the following general solution.

$$\xi(Y) = Ae^{\alpha Y} + Be^{-\alpha Y} + C\cos\beta Y + D\sin\beta Y \tag{2.12}$$

Where $\alpha = \sqrt{q^2 + q\sqrt{-P}}$, $\beta = \sqrt{-q^2 + q\sqrt{-P}}$

Next, we solve the Eq. (2.12) by taking into consideration the following boundary conditions:

1) $Y = 0$

At the base, the plate is fully bounded hence the w and the deflection angle, $\frac{dw}{dY}$ is assumed to be zero. Substituting $w = 0$, $\frac{dw}{dY} = 0$ into Eq. (2.12), we yield,

$$\xi = 0 \tag{2.13}$$

$$\xi' = 0 \tag{2.14}$$

2) When $Y = 1$

At the free end, the plate is unbounded, hence the bending moment, torque moment and shear force is zero. Eq. (2.15) represents the bending moment and Eq. (2.16) represents summation of the torque moment and shear force.

$$\xi'' - vq^2\xi = 0 \quad (2.15)$$

$$\xi^{(3)} - (2-v)q^2\xi' = 0 \quad (2.16)$$

Substituting the general solution Eq. (2.12) into Eqs. (2.13), (2.14), (2.15) and (2.16), we will yield a series of linear equations with coefficients *A, B, C* and *D*. These linear equations can be expressed in matrix form, **K** as shown below.

$$\mathbf{K} = \begin{bmatrix} 1 & 1 & 1 & 0 \\ \alpha & -\alpha & 0 & \beta \\ (\alpha^2 - vq^2)e^{\alpha} & (\alpha^2 - vq^2)e^{-\alpha} & -(\beta^2 + vq^2)\cos\beta & -(\beta^2 + vq^2)\sin\beta \\ [\alpha^2 - (2-v)q^2]\alpha e^{\alpha} & -[\alpha^2 - (2-v)q^2]\alpha e^{-\alpha} & [\beta^2 + (2-v)q^2]\beta\sin\beta & -[\beta^2 + (2-v)q^2]\beta\cos\beta \end{bmatrix}$$

$$\mathbf{K}\begin{bmatrix} A \\ B \\ C \\ D \end{bmatrix} = 0$$

When the determinant of matrix K is equals to 0, coefficients *A, B, C* and *D* will have multiple sets of solutions, in turn giving us a set of solutions for the minimum compressive stress *P* required for buckling. In other words, when the determinant of matrix K = 0, we can obtain the boundary between stable configuration and unstable configuration (buckling), as shown in the stability curve in Fig. 2-2 [2]. The curve is independent on of values of *l* and *h* and only varies with the Poisson's ratio.

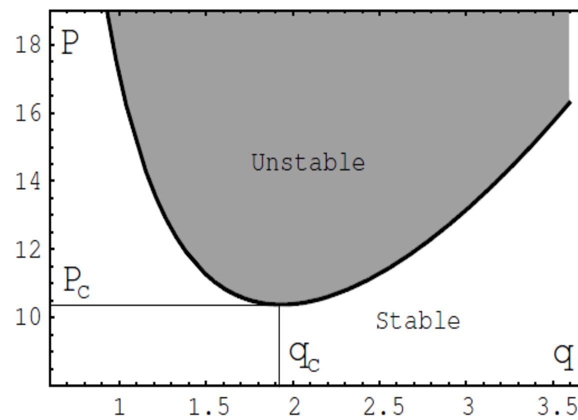

Fig. 2-2 Stability Diagram at Poisson's ratio =0.5, T.Mora [7].

P_c is the minimum compressive stress required for the buckling to occur and corresponding wavelength, q_c is obtained.

The results obtained from the stability diagram shall be used to validate the results from FEM analysis in the Chapter 2.3.

2.3 Finite element analysis of 1 Layer Model

2.3.1 Description of model schematics

Next FEM simulation is conducted and the results are compared with the theoretical equation to validate the suitability of the simulation models. The relationship between the width to height ratio *h/l*, the buckling stress $\sigma_{critical}$ and the relationship between is *h/l* and λ will be studied. However, prior to that, understanding how the total length of the model, *L* affects $\sigma_{critical}$ and λ will be crucial in setting the guidelines for when deciding the model schematics.

The 1 layer model created and the analysis conditions are shown in Fig. 2-3 and Table 2-1 respectively below.

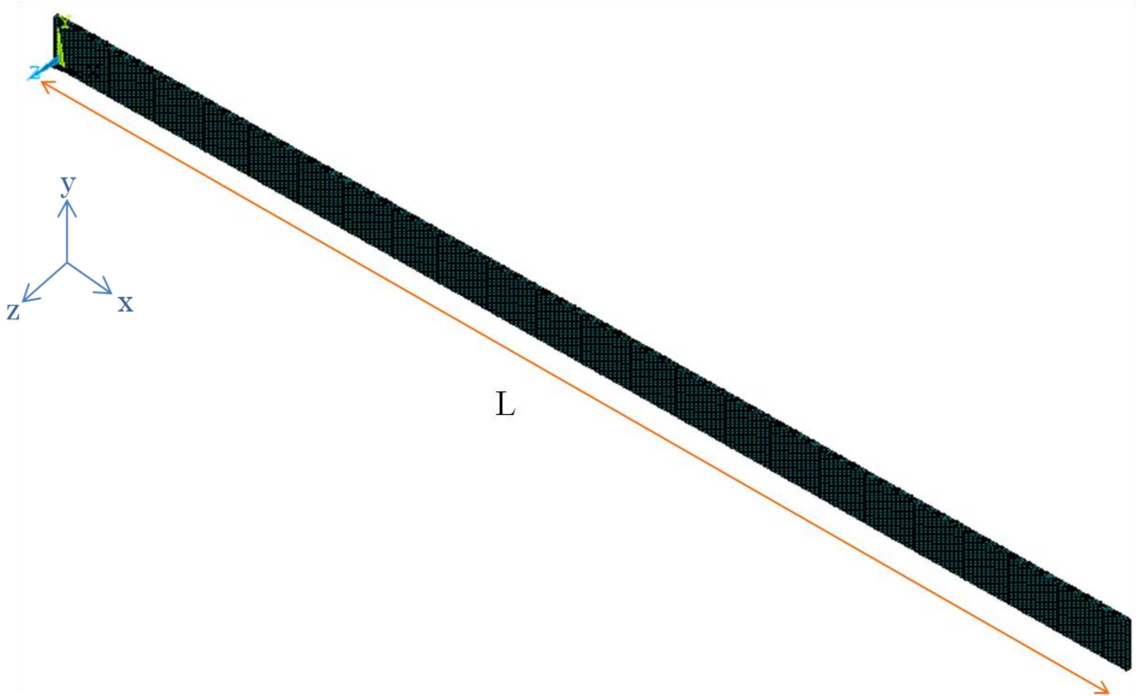

Fig. 2-3 Full 1 layer thin plate model.

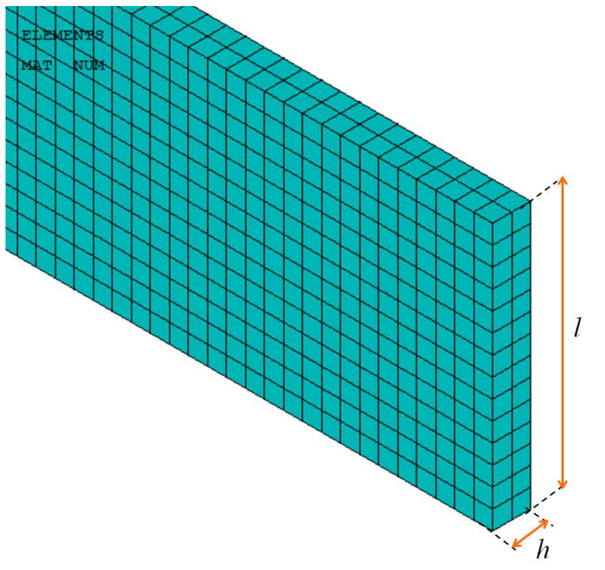

Fig. 2-4 Up close of one end of 1 layer model.

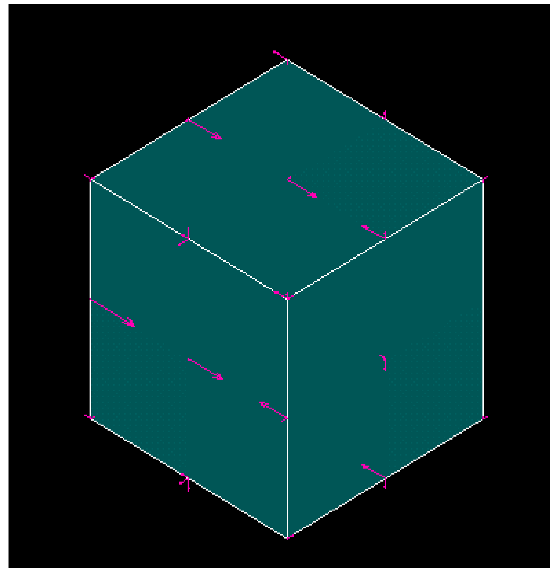

Fig. 2-5 Single element depicting intrinsic stress applies via inistate command.

Table 2-1 Finite Element Analysis Conditions.

Analysis software	Ansys 13.0
Units	[nm][N]
Number of nodes	114165
Number of elements	20000
Element type	20 Node Solid 186 (Inistate Stress Compatible)
Young's modulus	80GPa
Poisson's ratio	0.3
Type of analysis	Static/Eigen buckling
Boundary conditions	At Y=0, the model area is displacement X,Y, Z bounded
Force Conditions	1000MPa Compressive stress on all elements (see Fig. 2-6)

Upon application of intrinsic stress via the inistate command, static analysis considering the pre-stress effects is first conducted, followed by eigenbuckling analysis. Eigenbuckling analysis increases the unit stress applied in incremental sub steps till buckling occurs. $\sigma_{critical}$ and λ for the first buckling mode is then recorded. An example of the first buckling mode is shown in Fig. 2-6. One wavelength is the distance between 2 peaks/crests from the top view. Only the waves in

generated from the middle of the model, which exhibit constant wavelengths and amplitude, are measured as shown in Fig. 2-7. This is because the waves originating from the centre are the least affected by the boundary conditions both ends. The amplitudes of the wavelengths cannot be measured during eigenbuckling analysis as they are magnified multiple times and are not accurate.

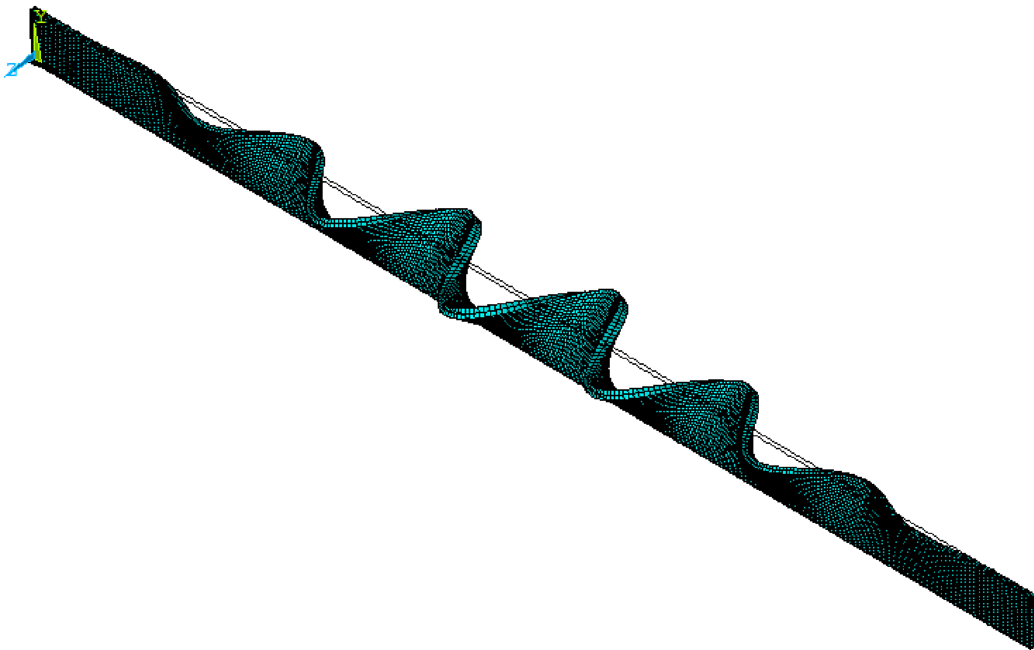

Fig. 2-6 First buckling mode of 1 layer model at $h/l = 0.1$.

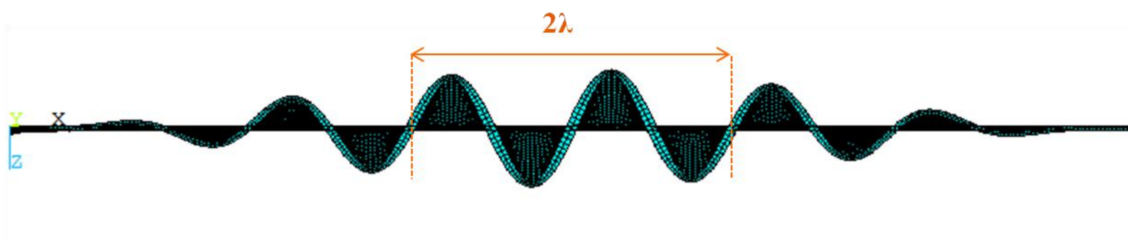

Fig. 2-7 Top view of buckled 1 layer model.

2.3.2 Assessment of the length for models

In semiconductors, the length of the plate, *L* is in order of microns while the height is in the order of nanometers. *L* is approximately close to a thousand times longer than its height. In theory, it is assumed that *L* is infinitely long. While it is ideal to conduct FEM simulation based on the full model length, this is difficult due to limitations in the software such as node limits and calculation time. If *L* is too short, the wavelength would be forced to be a multiple of *L*. Therefore, it is important to study the relationship that *L* and *l* have with $\sigma_{critical}$ and λ to optimize the *L* for thin plate models to be studied. *L* is first divided by *l* to make it dimensionless and the relationship between *L/l* ,$\sigma_{critical}$ and λ is studied.

The results of the relationship are shown below in Fig. 2-8.

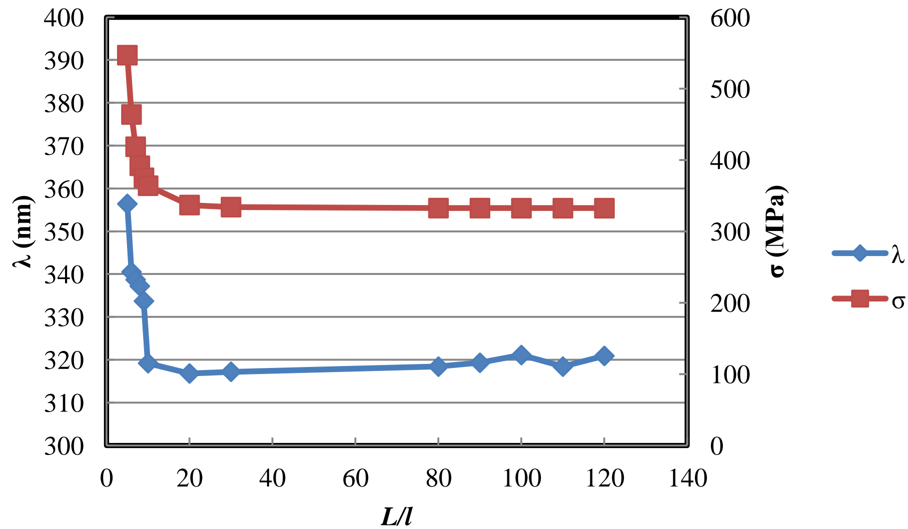

Fig. 2-8 Graph of $\sigma_{critical}$ and λ upon varying *L/l*.

As seen in Fig. 2-9, a small increase in *L/l* at low values causes significant decrease in both the

$\sigma_{critical}$ and λ values. After *L/l* crosses 20, both values of $\sigma_{critical}$ and λ stabilize and remain constant even as *L/l* continues to increase. The *L/l* ratio of models to be studied in this research will be greater than 20 to ensure sufficient accuracy in modeling thin plate behavior.

2.3.3 Comparison of simulation results with theoretical values at various width to height ratios

As mentioned in Chapter 2.1, in order for the Föppl von Kármán equations to stand, the height of plate, *l* must be significantly larger than the width of the plate, *h*. In other words, *h/l* must be sufficiently small. The relationship of *h/l* with the difference between the simulation and theoretical values are studied as shown in Fig. 2-9.

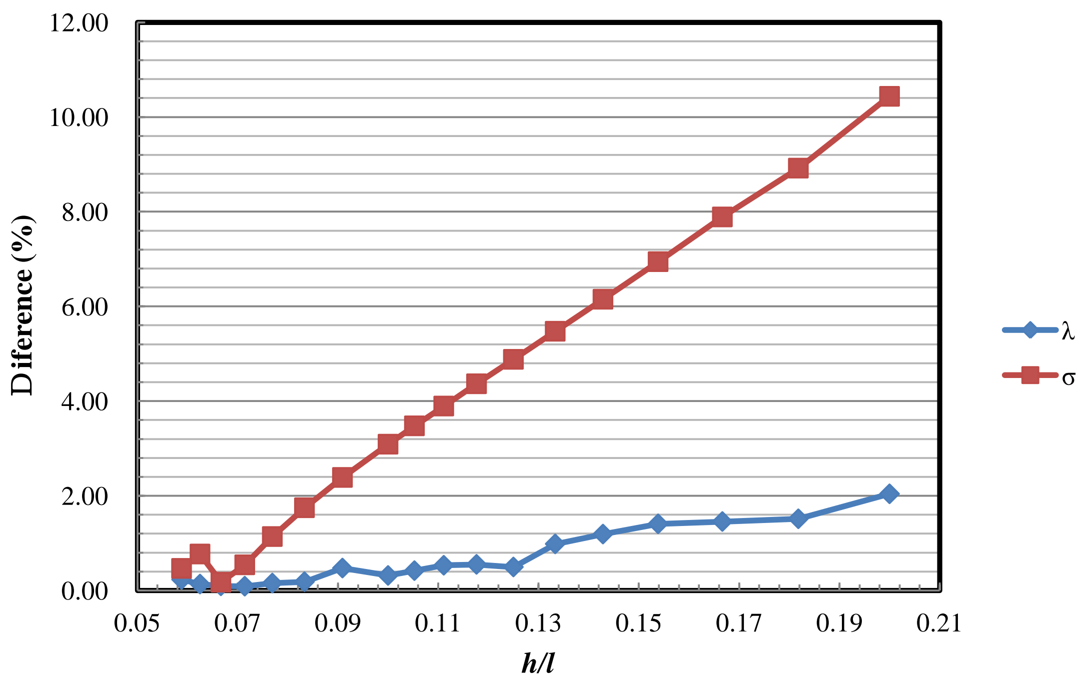

Fig. 2-9 Graph of difference between FEM and theoretical values of $\sigma_{critical}$ and λ at varying *h/l*.

As seen in Fig. 2-9, when *h/l* are increases beyond 0.08, both the percentage difference between FEM values and theoretical values for $\sigma_{critical}$ and λ increases. In particularly, the percentage difference for $\sigma_{critical}$ increased significantly with *h/l*. However when *h/l* equals to 0.08 and below, the percentage difference between FEM values and theoretical values is less than 1%. This is because as *h/l* decreases, assumptions for the Föppl von Kármán equations hold true and the FEM simulation results approach the theoretical results. As such, we can consider the FEM simulation results to be applicable at low values of *h/l*.

In conclusion, the FEM model created was able to predict $\sigma_{critical}$ and λ that are consistent with the theoretical values provided *L/h* is above 20. This also shows that FEM modeling might be sufficient to predict $\sigma_{critical}$ and λ at higher *h/l* ratios where the theoretical equations are not applicable.

Chapter 3. The 2 Layer Thin Plate Model

3.1 Introduction

The Föppl von Kármán equations can be modified to be applicable to the 2 layer model. However, the 2 layer model involves multiple correlated variables and numerical analysis must be conducted to verify the equation. At the current point of this research, very little past work has been done to apply the Föppl von Kármán equations to 2 layer plates.

This part of the research aims to focus on the FEM modeling aspect to study the characteristics of the buckling mechanism in order to provide insights to the establishment of the 2 layer theoretical equation.

Chapter 3.2 covers the description of the FEM 2 layer models and Chapter 3.3 will touch on the factors affecting $\sigma_{critical}$ and λ in 2 layer models.

3.2 Finite Element Analysis of 2 Layer Model

3.2.1 Description of model schematics

The general schematics of the 2 layer model to be analyzed are shown below in Fig. 3-1.

The measurement of $\sigma_{critical}$ and λ is the same as that of 1 layer models described in Chapter 2.3.1.

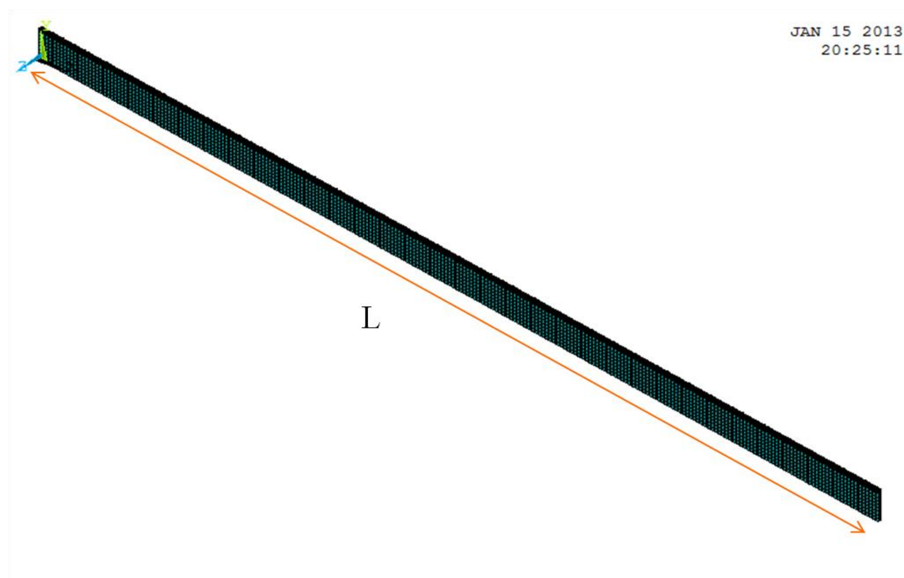

Fig. 3-1 Full 2 layer thin plate model.

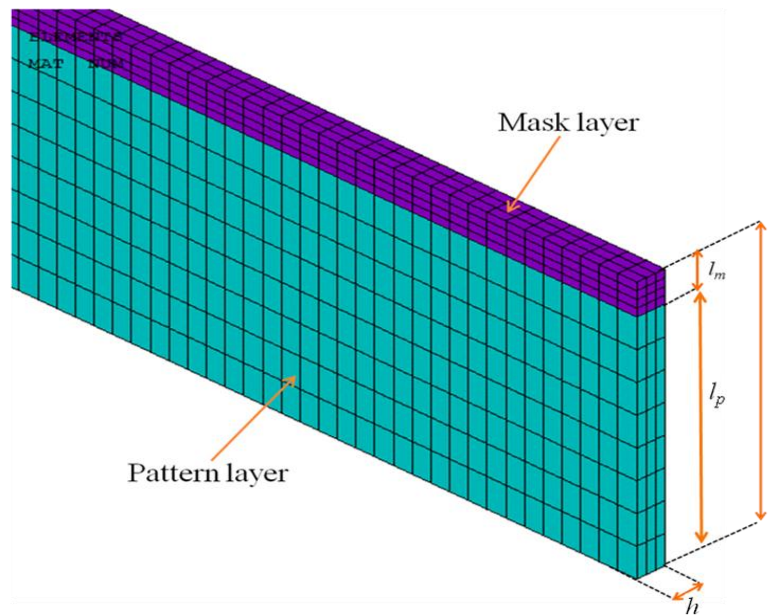

Fig. 3-2 Up close of one end of 2 layer model.

Table 3-1 FEM analysis conditions.

Analysis software	Ansys 13.0
Units	[nm][N]
Number of nodes	95639
Number of elements	18000
Element type	20 Node Solid 186 (Inistate Stress compatible)
Young's modulus of mask	122Gpa
Poisson's Ratio of mask	0.3
Young's modulus of pattern	12.8Gpa
Poisson's Ratio of pattern	0.3
Type of analysis	Static/Eigenbuckling
Boundary conditions	At Y=0, Displacement X,Y,Z bounded
Force conditions	1000MPa Compressive stress on Mask elements (shaded purple in Fig. 3-2)

3.2.2 Inconsistency of initial FEM results with experimental results

The experimental data used in this research was provided by Toshiba Corporate Engineering Manufacturing Center and recorded as shown in Table 3-2. Eight 2 layer models with varying total height l, mask height l_m and width h were patterned and fabricated. After fabrication, l, l_m, h and λ were measured from scanning electron microscope photographs.

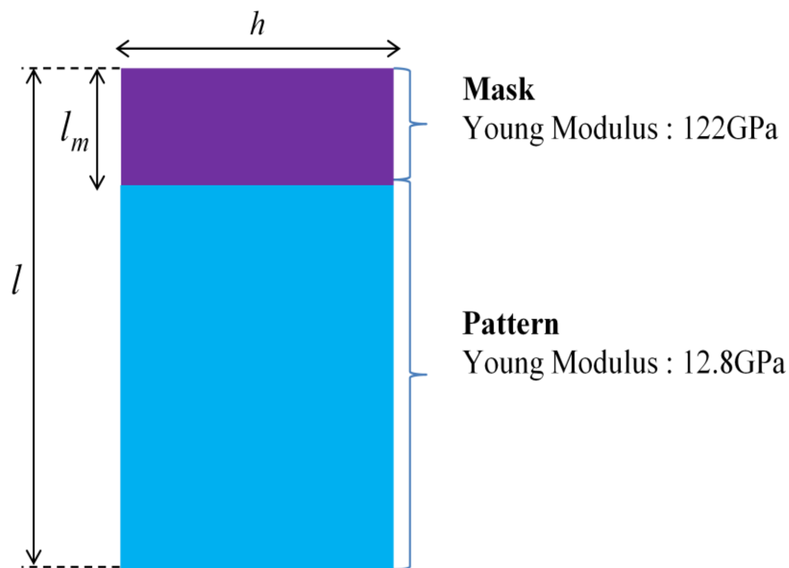

Fig. 3-3 Material Properties of 2 layer Model in experiments.

The residual stress present in the 2 layer plate is measured in a separate thin film experiment. A layer of thin film (mask) is deposited to a flat substrate (pattern) of uniform thickness. The substrate is initially stress-free but upon being bonded, residual stress is generated through the mechanisms mentioned in Chapter 1.1.3. The material properties of the substrate and thin film are known and by measuring the curvature of the substrate, the amount of stress generated can

be calculated using Stoney's equation, a formula relating curvature and stress [8]. The amount of stress recorded for this experiment is 927 MPa (compressive stress).

FEM analysis of 2 layer models based on the experimental data of l, l_m and h were conducted and the results for λ and $\sigma_{critical}$ were compared to the experimental results as shown below in Table 3-2.

Table 3-2 Comparison of experimental results and simulation results.

l_p	l_m	l	h	λ_{Exp}	λ_{FEM}	Difference	σ_{Exp}	σ_{FEM}	Difference
(nm)	(nm)	(nm)	(nm)	(nm)	(nm)	λ (%)	(MPa)	(MPa)	σ (%)

As seen in Table 3-2, there is a huge difference between FEM results and the experimental results for both λ and σ. For λ there are cases where more than a 100% difference exists between the experimental and FEM values. For the values of σ, some of the FEM values exceeded that of the experimental values, indicating that buckling should not have even taken place. We are also unable to draw any trends or conclusions from the results as multiple variables are being changed at any one time. In order to draw conclusions on whether this difference is due to wrong FEM analyzing methods or experimental error, we must first

understand the buckling phenomenon in 2 layer models, specifically, which variables affect $\sigma_{critical}$ and λ.

3.2.3 Discussion of areas of interest and governing factors

As the etching dept l (height of semiconductor element) increases, the structural changes can be classified into the two following variables:

1) The width to height ratio h/l decreases during etching as l increases and h remains constant;

2) The mask height to total height ratio l_m/l decreases as l_m remains constant while l increases

Fig. 3-4 below depicts the changes the variables undergo during the etching process. These two variables h/l and l_m/l are considered independent from one another and FEM simulation is conducted to study their relationship with $\sigma_{critical}$ and λ. Precaution was given to ensure that the range of values of h/l and l_m/l selected for FEM simulation encompasses the range of experimental values shown in Table 3-3.

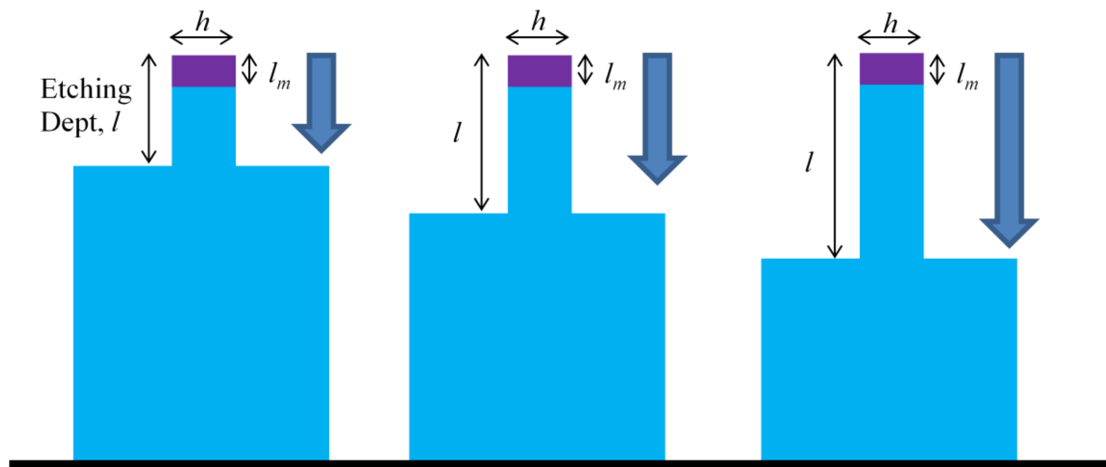

Fig. 3-4 Change in variables during semiconductor etching process.

Table 3-3 h/l and l_m/l of experimental results.

l_p (nm)	l_m (nm)	l (nm)	h (nm)	h/l	l_m/l

3.3 Factors affecting λ and $\sigma_{critical}$

3.3.1 Relationship of λ and $\sigma_{critical}$ with respect to h

h is varied while keeping l and l_m/l constant. The relationships are plotted in Fig. 3-5 shown below.

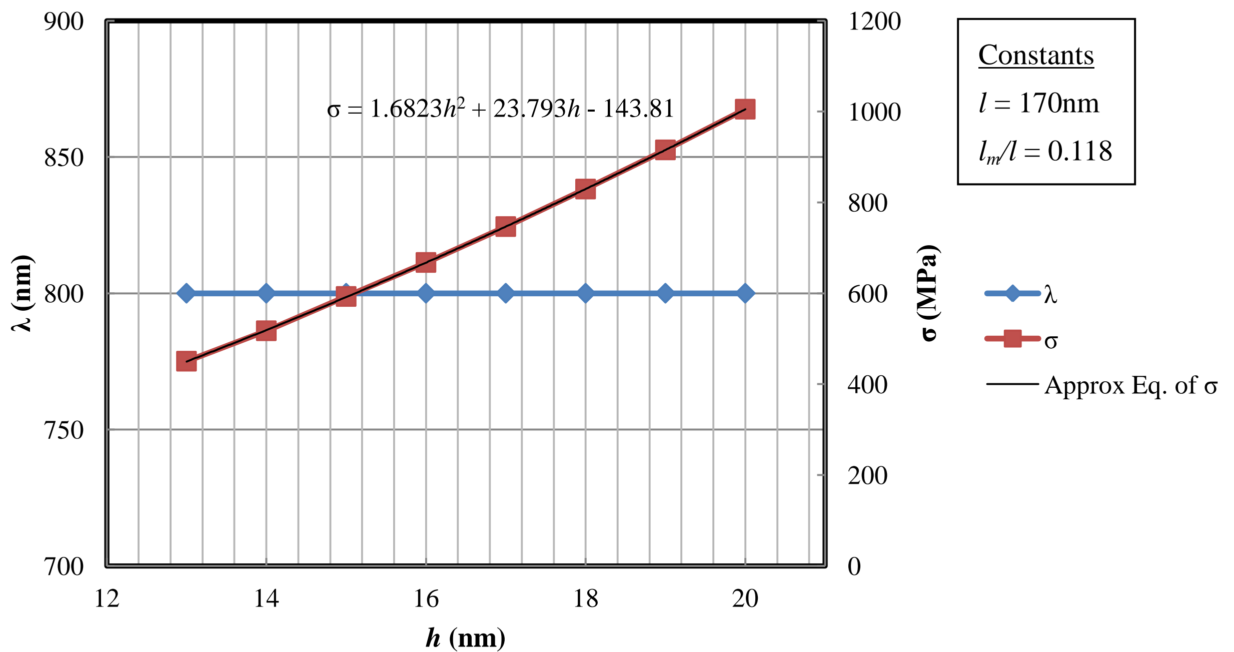

Fig. 3-5 Graph of λ and $\sigma_{critical}$ upon varying h.

λ and h: According to Fig. 3-5, λ remains constant despite increasing values of h This shows that λ is independent of h, but it is still inconclusive to whether λ is independent of h/l. In the next sub chapter, l will be varied and h will be kept constant.

$\sigma_{critical}$ and h: According to Fig. 3-5, $\sigma_{critical}$ increases significantly when h increases. An increase in h increases the overall bending stiffness of the model, resulting in a higher $\sigma_{critical}$. A second order polynomial equation can be approximated from the $\sigma_{critical}$ and h curve, showing

that $\sigma_{critical}$ is proportional to the square of h. According to Eq. (2.8), $\sigma_{critical}$ should vary proportionally to the square of h/l. As l is kept constant in the simulation, it is conclusive that the FEM simulation results concur with the Föppl von Kármán equations for the 1 layer model.

3.3.2 Relationship of λ and $\sigma_{critical}$ with respect to l

In this next study, l is varied (while keeping l_m/l and h constant) and its relationship with λ and $\sigma_{critical}$ was studied. The relationships are plotted in Fig. 3-6 shown below.

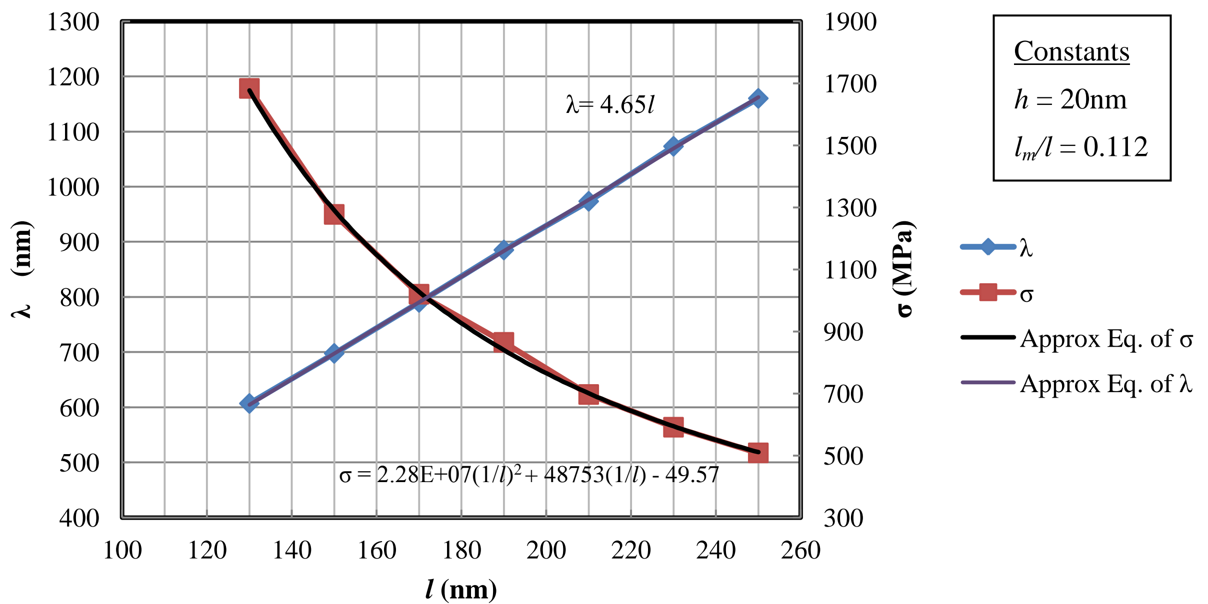

Fig. 3-6 Graph of λ and $\sigma_{critical}$ upon varying l.

λ and l: According to Fig. 3-6, an increase in l causes λ to increase linearly. Combing this data with those in Fig. 3-4, we can conclude that λ is independent of h and has a linear relationship with l. Referring to Eq. (2.10), this concurs with the Föppl von Kármán equations for the one

layer model.

$\sigma_{critical}$ and *l*: According to Fig. 3-6, $\sigma_{critical}$ increases significantly when *l* increases. As the mask layer at the top of the model contributes the main compressive force, an increase in *l* causes this compressive force to be located further away from the bounded region. This result in an overall lowered bending stiffness of the model and thus lowers $\sigma_{critical}$.

A second order polynomial equation can be approximated from the $\sigma_{critical}$ and *l* curve, showing that $\sigma_{critical}$ is inversely proportional to the square of *l*. According to Eq. (2.8), $\sigma_{critical}$ should vary proportionally to the square of *h/l*. Hence, it is conclusive that the FEM simulation results concur with the Föppl von Kármán equations for the 1 layer model.

3.3.3 Relationship of λ and $\sigma_{critical}$ with respect to l_m/l

Next, l_m/l was varied (while keeping h/l constant) and its relationship with λ and $\sigma_{critical}$ was studied. The relationships are plotted in Fig. 3-6 shown below.

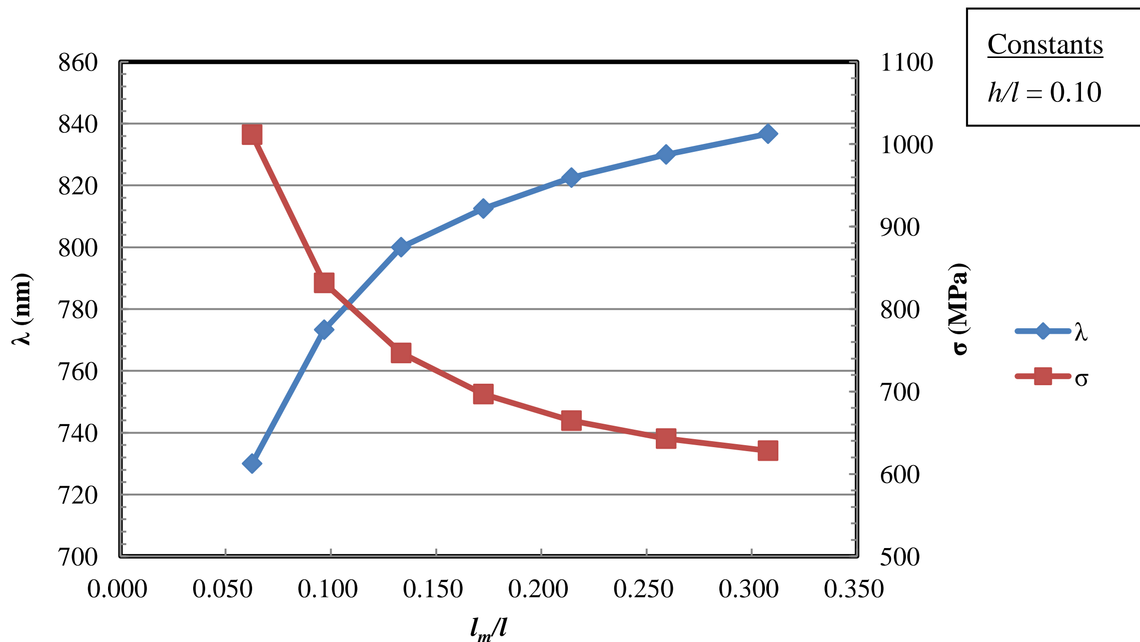

Fig. 3-7 Graph of λ and $\sigma_{critical}$ upon varying l_m/l.

λ and l_m/l: In general, an increase in l increases causes λ to increase. The rate of increase of λ appears to slow down as l_m/l reaches the values above 0.250.

$\sigma_{critical}$ and l_m/l: Initially, $\sigma_{critical}$ decreases significantly when l_m/l increases. However, similar to λ, the rate of decrease seems to slow down as l_m/l reaches the values above 0.250. As the mask layer contributes the primary source of compressive force, when the ratio of l_m to l is increased, the amount of compressive force per unit length is increased. A greater compressive force would result in a lower $\sigma_{critical}$.

Chapter 4. Comparison of experimental and FEM results

4.1 Introduction

As we know, the experimental results and FEM simulation results greatly differed as shown in Table 3-2. One of the possible reasons is that buckling has occurred at a value of l that is lower than that of l recorded in the experimental results. The experimental values of l were only recorded after the whole fabrication process was finished. This means that there is a possibility that buckling has occurred at a lower value of l earlier during the etching process. If this is the case, the simulation of the model based on a larger value of l would naturally yield incorrect results. Let us refer to the value of l that buckling occurs at as l_{critical} and the value of l that has been recorded in the experiment as l_{final}. This chapter serves to explore the procedures and limitation involved in finding l_{critical}.

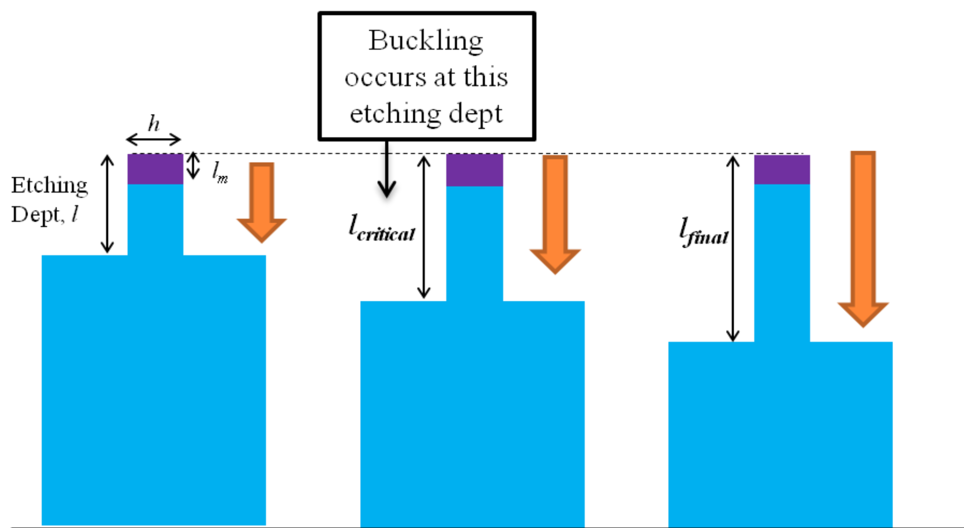

Fig. 4-1 Figure showing the etching process at which when l_{critical} occurs.

4.2 Finding the values $l_{critical}$

4.2.1 Relationship between λ/l and l_m/l

As we have seen in Chapter 3.4, λ varies linearly with l and is independent of h. By dividing λ with l, we arrive at a dimensionless variable, λ/l. Regardless of the values of h and l, a constant relationship between λ/l and l_m/l should exist.

FEM simulations of multiple values of h/l were taken and the relationship between λ/l and l_m/l is plotted as shown in Fig. 4-2 below. Assuming that the model is not beyond that of a thin plate, the results concur that there exists a constant relationship between λ/l and l_m/l.

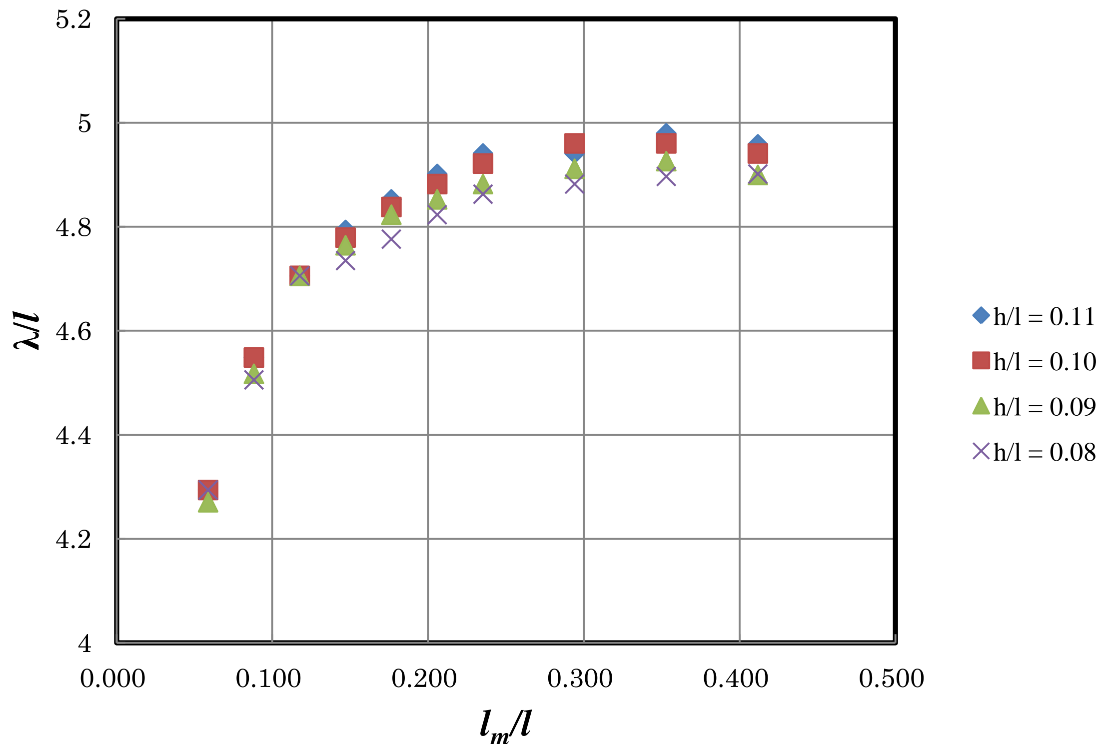

Fig. 4-2 Graph of relationship between λ/l and l_m/l at various h/l.

Next, the experimental values of λ/l and l_m/l were plotted on the same axes with the results from FEM in Fig. 4-3 below. It can be observed that the experimental results exhibit the same trend as the FEM results but at a lower value of λ/l and l_m/l. This affirms our suspicion that the buckling occurs at a lower value than the l_{final}. If the values of l in the experimental results are smaller than l_{final}, λ/l and l_m/l of the experimental results will increase and may approach values obtained from FEM.

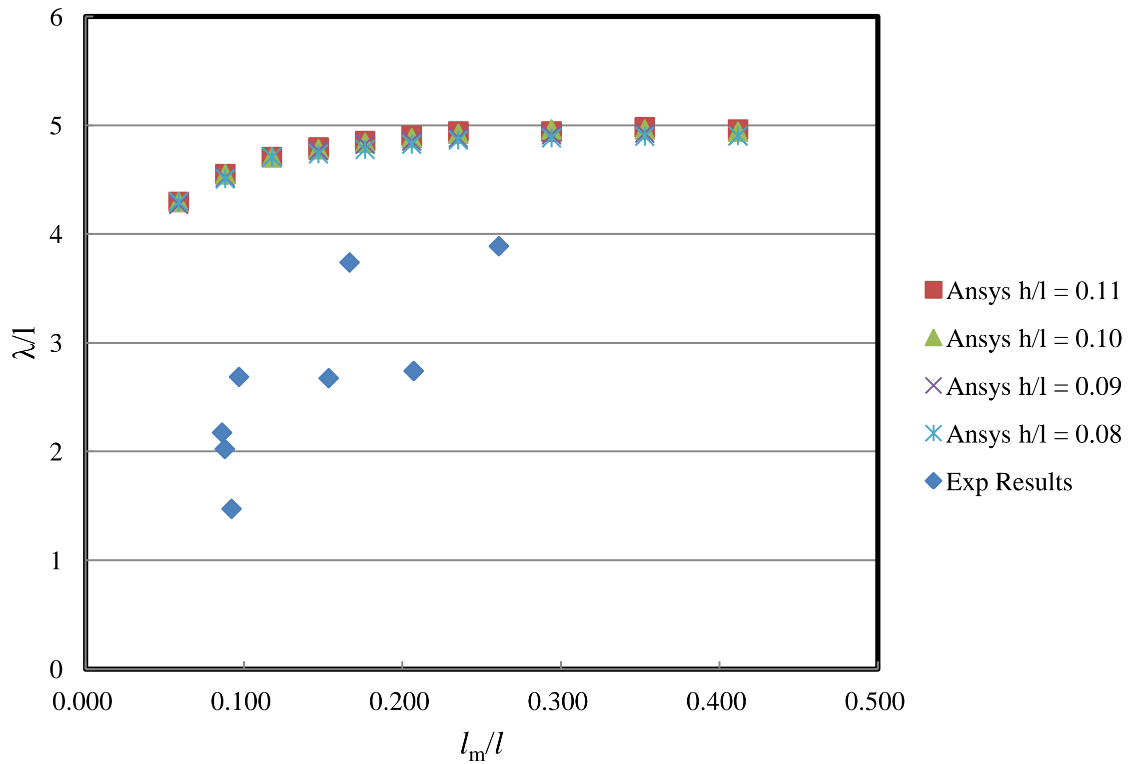

Fig. 4-3 Graph of relationship between λ/l and l_m/l for experimental and Ansys (FEM) results.

4.2.2 Calculating $l_{critical}$ from λ and l_m relationships

Given the constant relationship between λ/l and l_m/l, the next step is to find an equation relating λ, l_m and l. The average values of λ/l at different width to height ratios are taken and plotted against l_m/l. A fifth order polynomial equation, Eq. (4.1) can then be approximated from the curve within the range of ($0.05 < l_m/l < 0.42$).

$$\frac{\lambda}{l} = C_1\left(\frac{l_m}{l}\right)^5 + C_2\left(\frac{l_m}{l}\right)^4 + C_3\left(\frac{l_m}{l}\right)^3 + C_4\left(\frac{l_m}{l}\right)^2 + C_5\left(\frac{l_m}{l}\right) + C_6 \tag{4.1}$$

Where C_1 to C_6 are coefficients of the approximated equation.

Eq. (4.1) can be rearranged to give the following form below.

$$C_6 l^5 + (C_5 l_m - \lambda) l^4 + C_4 l_m^2 l^3 + C_3 l_m^3 l^2 + C_2 l_m^4 l + C_1 l_m^5 = 0 \tag{4.2}$$

Values of l_m and λ are substituted into Eq. (4.2) and the Newton-raphson method is used predict the values of $l_{critical}$.

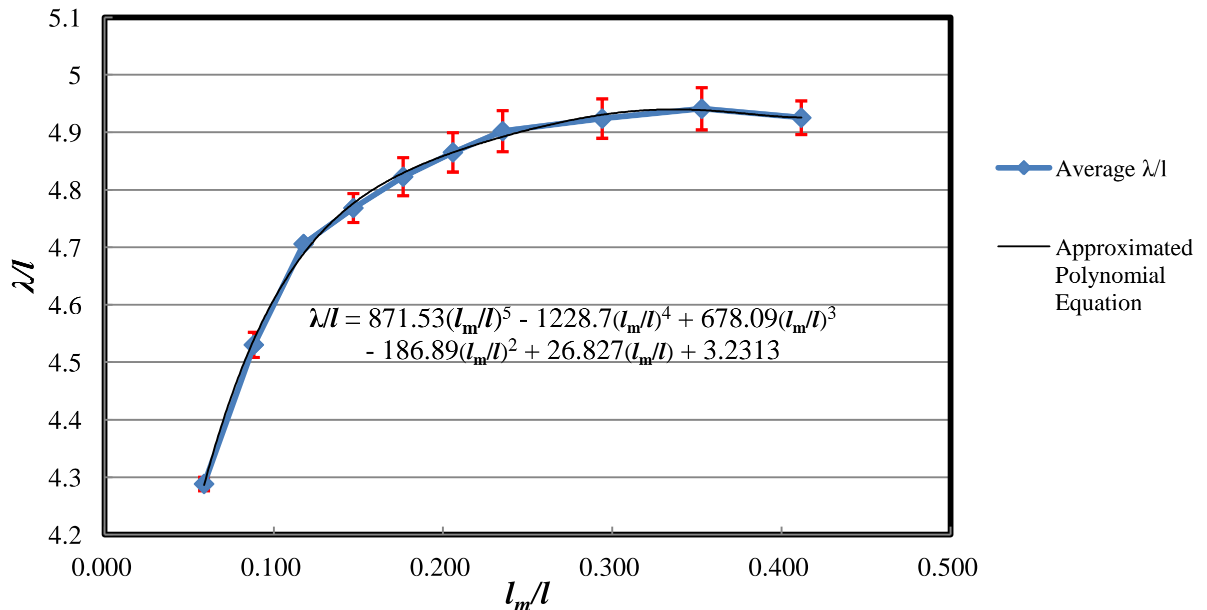

Fig. 4-4 Graph of average λ/l against l_m/l with error bars.

4.2.3 Discussion of results for $l_{critical}$ obtained from l (l_m, λ)

Next, FEM simulations of models with values of $l_{critical}$ were conducted in order to confirm their accuracy. The results of the simulation are shown below in Table 4-1.

Table 4-1 Predicted values of $l_{critical}$ and the corresponding $\sigma_{critical}$.

l_m (nm)	h (nm)	l_{final} (nm)	$l_{critical}$ (nm)	λ_{exp} (nm)	λ_{FEM} (nm)	$\sigma_{critical}$ (MPa)
31.0	25.0	202.0	109.6	540	560	2685
33.0	28.0	198.0	151.7	740	760	1931
24.0	26.0	273.0	113.3	552	570	2794
28.0	29.0	289.0	160.8	776	797	1934
30.0	23.0	115.0	90.5	447	465	3197
35.0	23.0	169.0	93.8	463	480	3028
26.0	23.0	282.0	84.1	415	435	3602
25.0	28.0	290.0	129.9	630	650	2558

The values of λ_{FEM} were close to that of λ_{exp}, however the FEM values of $\sigma_{critical}$ were significantly higher than the amount of stress present in the mask layer during the experiment. As mentioned earlier in Chapter 3.1, the amount of stress recorded in the mask layer during the experiments is 927MPa. Most of these results are at least 2-3 times larger than this value, meaning that based on these values of $l_{critical}$, the buckling should not have occurred in the experiments.

One of the possible reason to explain the why the values of $\sigma_{critical}$ obtained are significantly greater than the amount of stress recorded in the experiment is that λ_{exp} is not the wavelength at

which buckling occurs. In other words, the wavelength does not remain constant as the etching depth is increased from $l_{critical}$ to l_{final}. As we substituted this value of λ_{exp} into Eq. (4.2), the values of $l_{critical}$ obtained would be inaccurate.

Assuming that this is true and λ_{final} (wavelength at l_{final}) is not equals to the $\lambda_{critical}$ (wavelength at point of buckling), we need to affirm this by finding $l_{critical}$ from the relationship between $\sigma_{critical,}$ l_m and l.

4.2.4 Calculating $l_{critical}$ from $\sigma_{critical}$ and l_m

In this sub chapter, we shall attempt to find the value of $l_{critical}$ from the relationship between $\sigma_{critical,}$ l_m and l. Similar to what we did for λ, we can obtain this equation in two ways: 1) Making $\sigma_{critical}$ dimensionless variable that is unaffected by h/l or l_m/l and then approximating the equation; 2) finding the function of the surface in a 3D scatter plot of $\sigma_{critical}$, l_m/l and h/l.

As we can see from the 3D surface graph below in Fig. 4-5, the relationship between $\sigma_{critical,}$ l_m and l is complex and unlike λ which can be made dimensionless easily (λ is proportional to l), $\sigma_{critical,}$ does not exhibit any linear relationship with any of the variables. As such, we adopted method 2 in trying to find the governing equation.

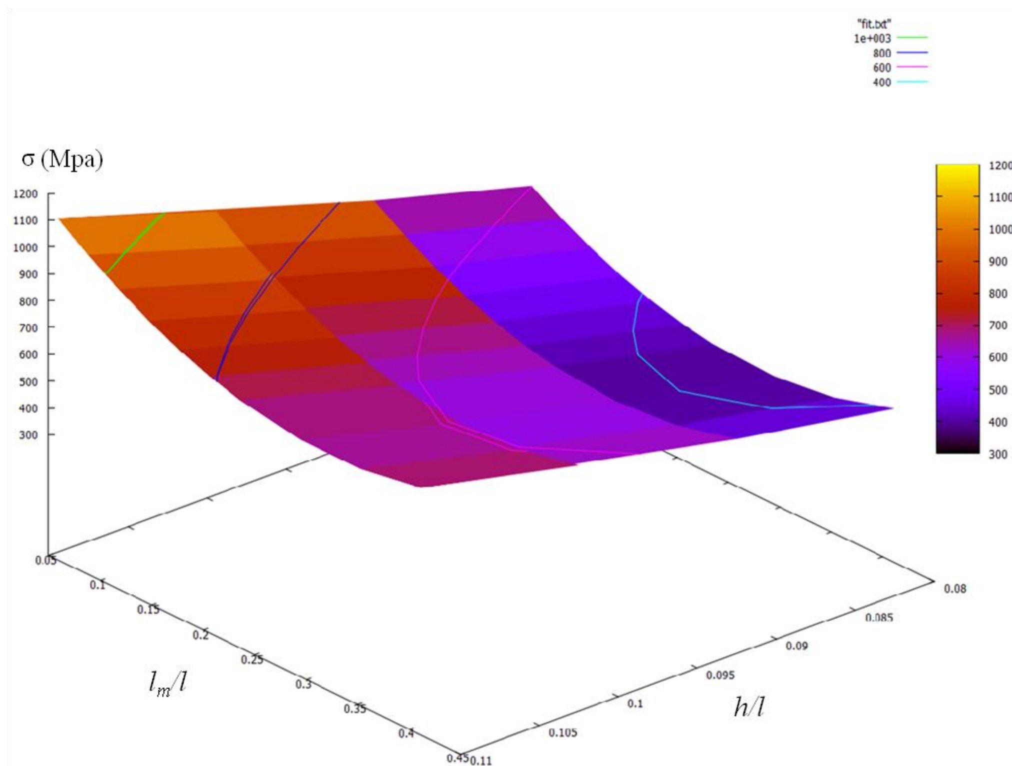

Fig. 4-5 3D surface graph of $\sigma_{critical}$, l_m/l and h/l.

Method 2 involves fitting the data into a function and there exists many different ways to do so. In order to keep things simple, the least squared regression fitting was used to summarize the relationship between l_m/l and h/l. The least squared method creates a polynomial function where the sum of the squares of the residuals (difference between observed value and predicted value) is kept at its minimum [9]. The polynomial function created will take the form shown below in Eq. (5.1).

$$\sigma\left(\frac{h}{l},\frac{l_m}{l}\right) = A + B\left(\frac{h}{l}\right) + C\left(\frac{l_m}{l}\right) + D\left(\frac{h}{l}\right)^2 + E\left(\frac{l_m}{l}\right)^2 + F\left(\frac{h}{l}\right)\left(\frac{l_m}{l}\right) \quad (5.1)$$

where A, B, C, D, E and F are coefficients

We can obtain the values of $l_{critical}$ by substituting in the experimental values of l_m, h and the σ (927MPa) into Eq. (5.1) and solving for l.

4.2.5 Discussion of results of obtained from σ (l_m, h, l)

Table 4-2 Predicted values of $l_{critical}$ and the corresponding $\lambda_{critical}$.

l_m (nm)	h (nm)	l_{final} (nm)	$l_{critical}$ (nm)	$l_{critical}/l_{final}$	λ_{final} (nm)
31	25	202.0	227.3	1.13	540.0
33	28	198.0	256.7	1.30	740.0
24	26	273.0	247.4	0.91	552.0
28	29	289.0	274.2	0.95	776.0
30	23	115.0	207.3	1.80	447.0
35	23	169.0	201.9	1.19	463.0
26	23	282.0	212.3	0.75	415.0
25	28	290.0	267.7	0.92	630.0

As seen in Table 4-2, the values of l_{critical} are significantly larger than that of $l_{\text{final.}}$ As such, we are unable to confirm our suspicions that λ_{final} is not equals to the $\lambda_{\text{critical}}$.

By manipulating Eq. (5.1) and making l the subject, we can arrive at Eq. (5.2).

$$l_{critical} = \frac{-(\mathrm{B}h + \mathrm{D}l_{\mathrm{m}}) \pm \sqrt{(\mathrm{B}h + \mathrm{D}l_{\mathrm{m}})^2 - 4(\mathrm{A} - \sigma)(\mathrm{C}h^2 + \mathrm{E}l_{\mathrm{m}}^2 + \mathrm{F}hl_{\mathrm{m}})}}{2(\mathrm{A} - \sigma)} \qquad (5.2)$$

We can see that l_{critical} is proportional to $\frac{h}{\sqrt{\sigma}}$. A decrease in values of h or an increase of σ could have caused the values of l_{critical} to be greater than it should be.

Some of the possible reasons of why the experimental data does not match the simulation data are as follows:

1) There exist initial imperfections in the structure. According to experimental results, there is a 2-3nm variation on each end of the width along the whole length of the semiconductor element. That results in a total of a 4-6nm variation for h when both ends are considered. The experimental values of h recorded are the average width measured where the mask and pattern meets. However, the sample size is small and the deviation is large. A difference in 5nm would account for close to a 20% difference in the experimental values of h recorded in Table 4-2. According to Eq. (5.2), l_{critical} is proportional to h and a 20% decrease in h would also result in a 20% decrease in the l_{critical} calculated. As such, there is a need to increase the number of samples for the width to ensure a more accurate value of l_{critical}.

2) The mask layer (amorphous silicon) could have undergone oxidation during the fabrication process resulting in a greater stress than 927MPa. According to Eq. (5.2), $l_{critical}$ is inversely proportional to the root of σ and an increase in σ would decrease $l_{critical}$. This effect is however considered negligible.

3) Through the process of etching, h does not remain constant at various etching depths. Possibly due to existing structural imperfections or the reflection of gas molecules during the etching process causing the walls of the element are eroded away. h is both a function of the current etching depth, $l_{current}$ and its relative depth l as seen in Fig. 4-6. As h changes, this would definitely affect the stress σ and depth at which it buckles $l_{critical}$.

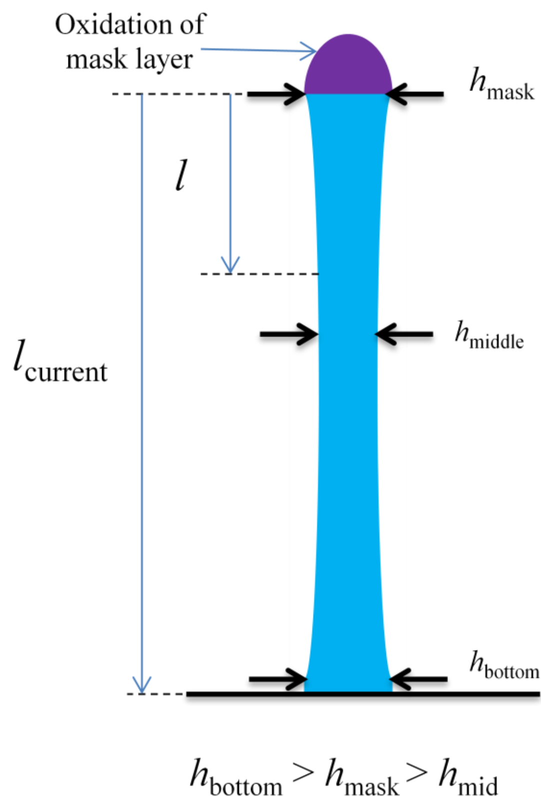

$$h_{bottom} > h_{mask} > h_{mid}$$

Fig. 4-6 Change in h according to etching depth l.

Chapter 5. Conclusion

5.1 Summary of results

In aim of improving the framework for the design of semiconductor nanoscale structures to prevent buckling phenomenon, this research has made clear the characteristics of the buckling mechanism in 2 layer thin plates and the factors affecting the buckling wavelength and stress through FEM simulation.

The stress at which buckling occurs, $\sigma_{critical}$ is inversely proportional to the $(h/l)^2$ and decreases non-linearly to l_m/l. Through data fitting between the range of values where $0.08<h/l<0.11$ and $0.05<l_m/l<0.41$, a model capable of predicting the length at which buckling occurs, $l_{critical}$ given that the stress present in the mask layer, l_m and the h is known. Vice versa, if $l_{critical}$ is known, the stress present in the mask layer can be predicted.

The wavelength λ is independent of h, linearly proportional to l and increases non-linearly to an increasing l_m/l. As such, by making λ dimensionless in the form of λ/l, a fixed relationship between λ/l and l_m/l, independent of values of h/l can be obtained. From this constant relationship, we are able to obtain a model that is able to predict $l_{critical}$ given that the wavelength at which buckling occurs $\lambda_{critical}$, l_m and the h is known. Vice-versa, if $l_{critical}$ is known, $\lambda_{critical}$ can be predicted.

From this two prediction models, given either $\lambda_{critical}$ or $\sigma_{critical}$ is known, we are able to predict the other unknown.

Unfortunately, the experimental results were insufficient and the limitations of the current FEM modeling were made clear. More experimental results could be taken to correctly estimate the height, lateral shape, and wavelength of the element at the point of buckling.

5.2 Suggestions for future research

1. Föppl von Kármán equation for 2 layer thin plates.

   The Föppl von Kármán equations can be modified to be applied on 2 layer models and the theoretical results can be compared to the experimental results.

2. Additional experiments need to be conducted and the current FEM results should be evaluated once more as the current experimental data does not accurately estimate the height, lateral shape, and wavelength of the element at the point of buckling. The additional experiments should be conducted where images captured are at different etching depth intervals.

3. FEM modeling based on reducing pattern width at increasing etching heights.

   As mentioned in Chapter 4.2.5, the pattern width seems to be a function of the etching depth and the relative depth. New FEM modeling is required to find out how this change in pattern width affects the wavelength and buckling stress.

References

[1]. L.B.Freund, S.Suresh, Thin Film Materials Stress Defect Formation and Surface Evolution, United Kingdom Cambridge University Press IBSN 0-521-82281-5 (2003)

[2]. Gordon Moore, The Future of Integrated Electronics, Fairchild Semiconductor internal publication (1964).

[3]. B. Arnold, Shrinking Possibilities, Institute of Electrical and Electronics Engineers (IEEE) Publication, April 2009

[4]. Evans, A.G, Hutchinson J.W, The thermochemical integrity of thin film and multilayers, Acta Metall, Mater **43**, 1411-1428

[5]. M.Darnon, T. Chevolleau, O. Joubert, Undulation of sub-100nm porous dielectric structures: A mechanical analysis, Applied Physics Letters **91**, 194-103 (2007)

[6]. T. Mora, A. Boudaoud, Buckling of swelling gels, The European Physical Journal E **20**, 119-124(2006)

[7]. 長谷川，　弾性安定の理論，ブレイン図書出版, 303-328 (1974)

[8]. Stoney, G.G, The tension of metallic films deposited by electrolysis, Proceeding of the Royal Society (London) **A82**, 172-175 (1909)

[9]. Bishop C. M., Pattern Recognition and Machine Learning, Springer IBSN 0-387-31073-8 (2006)

Acknowledgements

I would like to express my heartfelt gratitude to Professor Shinsuke Sakai and Professor Satoshi Izumi for giving me the chance to conduct research at their laboratory.

I would also like to extend my sincere gratitude to Mr Keiji Suzuki, Ms. Sachiyo Ito and Mr Keisuke Unosawa from Toshiba Corporate Engineering Manufacturing Center for their continual support and useful insights to semiconductor fabrication techniques.

I would like to express my sincere thanks to my thesis advisor Professor Izumi for advice and help throughout the course of my research. To my associate Professor Hiro Tanaka, I would like to express my gratitude and thanks for his constant guidance and extraordinary patience. This thesis would not have been possible without both Professor Izumi's and Associate Professor Tanaka's guidance. In addition, thank you to my senior, Master's student Takahiro Hidaka for his constant support and brilliant advice throughout this past six months.

Despite being a foreigner, I would like to thank all the laboratory members for being kind, friendly and welcoming towards me. I have never felt a moment of being out of place around all of them.

p.1~p.55 完

平成25年2月1日提出

110203　シー　ロンチュン